

Multiple Dirac Cones and Topological Magnetism in Honeycomb-Monolayer Transition Metal Trichalcogenides

Yusuke Sugita,¹ Takashi Miyake,² and Yukitoshi Motome¹

¹Department of Applied Physics, University of Tokyo, Bunkyo, Tokyo 113-8656, Japan

²CD-FMat, National Institute of Advanced Industrial Science and Technology (AIST), Tsukuba, Ibaraki 305-8568, Japan

The discovery of monolayer graphene[1] has initiated two fertile fields in modern condensed matter physics, Dirac semimetals and atomically-thin layered materials. When these trends meet again in transition metal compounds, which possess spin and orbital degrees of freedom and strong electron correlations, more exotic phenomena are expected to emerge in the cross section of topological states of matter and Mott physics. Here, we show by using *ab initio* calculations that a monolayer form of transition metal trichalcogenides (TMTs), which has a honeycomb network of transition metal cations, may exhibit multiple Dirac cones with tunable gaps in the electronic structure. Furthermore, we elucidate that electron correlations and carrier doping turn the multiple-Dirac semimetal into a topological ferromagnet with high Chern number. Our findings raise the honeycomb-monolayer TMTs to a new paradigm to explore correlated Dirac electrons and topologically-nontrivial magnetism. In turn, the unique wide-ranging properties of the materials will deliver new building blocks for atomically thin heterostructures.

Since the success of exfoliation of a monolayer graphene[1], atomically-thin layered materials have grown as one of the leading themes in modern condensed matter physics. In particular, van der Waals (vdW) materials, composed of atomic layers bounded via weak vdW forces, have received great attention. Electrons confined in an atomically thin layer exhibit drastically distinct behaviour from the bulk form. The archetypal example is the Dirac electrons in a monolayer graphene, which show anomalous transport behaviour, e.g., the anomalous integer quantum Hall effect and the Klein tunneling[1, 2]. Another example is the valley degree of freedom in the monolayer form of transition metal dichalcogenides[3], which has been intensively studied toward valleytronics devices[4, 5]. Furthermore, heterostructures of different vdW materials have provided a new platform for novel functionalities never seen in bulk compounds[6, 7].

Through the intensive research in the past decade, a lot of efforts have been made to find atomically-thin *magnetic* materials. Among many candidates, a family of transition metal trichalcogenides (TMTs) has gained increasing interests, both from theoretical proposals of monolayer magnetism[8, 9] and experimental reports on the mono and few-layer forms[10–13]. In addition, not only the magnetism but also anomalous electronic and transport properties are predicted in the presence of the relativistic spin-orbit cou-

pling (SOC), e.g., the spin-valley coupling[14], the magnon spin Nernst effect[15], and the gate-controllable magneto-optic Kerr effect[16]. Thus, the atomically-thin layered TMTs are expected to provide a unique cross section between strong electron correlations and the SOC, but their potential remains unexplored. In this work, we theoretically propose that monolayer TMTs with a honeycomb network of *4d* and *5d* transition metals would host a new playground for correlated Dirac electrons and topologically-nontrivial magnetism.

The chemical formula for TMTs is generally given by MBX_3 , where M is transition metals, $B=P, Si, \text{ or } Ge$, and X is chalcogens. TMTs have vdW layered structures, whose stacking manner depends on the compounds[17–20]. In each layer, transition metal cations M comprise a honeycomb network by sharing the edges of MX_6 octahedra, and B_2 dimers locate at the centers of the hexagons of the honeycomb network (Fig. 1a). The nominal valence of the transition metal cation is M^{2+} ; for instance, some 10- and 12-group elements can take the stable divalent oxidation state[21], and indeed, MPX_3 with $M=Ni, Pd, Zn, Cd, \text{ and } Hg$ have been synthesized[17]. In the following, we focus on monolayer TMTs with 10-group elements, MPX_3 with $M=Ni, Pd, \text{ and } Pt$.

First, we calculate the electronic band structures in the paramagnetic state by *ab initio* calculations without the SOC (see Method for details). Figures 1b,c show the representative results for $PdPS_3$. The band structure shows that the $Pd\ d$ -orbital levels are split into two groups, e_g and t_{2g} , due to the crystalline electric fields of octahedral ligands. As Pd^{2+} is in the d^8 electron configuration, the lower-energy t_{2g} manifold is fully occupied and the higher-energy e_g manifold is half-filled. Remarkably, the e_g bands have two crossing points at the K point and around the midpoint on the Γ -K line in the Brillouin zone, and the projected density of states are almost zero at the Fermi level. We find that the crossings are the Dirac cones, as shown in Fig. 1d: two electronic bands near the Fermi level give rise to eight Dirac cones (two independent ones on the zone boundary, K and K', and other six inside). We confirm that the multiple Dirac cones are shared by other monolayer TMTs with $M=Ni, Pd, \text{ and } Pt$ (see Supplementary information).

In order to clarify the microscopic origin of the multiple Dirac cones, we construct the maximally localized Wannier functions (MLWFs)[22, 23] for the e_g bands and evaluate the overlap integrals between them. Figures 2a,b show the MLWFs obtained from two initial states, $d_{3z^2-r^2}$ and $d_{x^2-y^2}$, respectively. Both MLWFs well extend over the neighbouring S sites, indicating the importance of indirect hopping processes

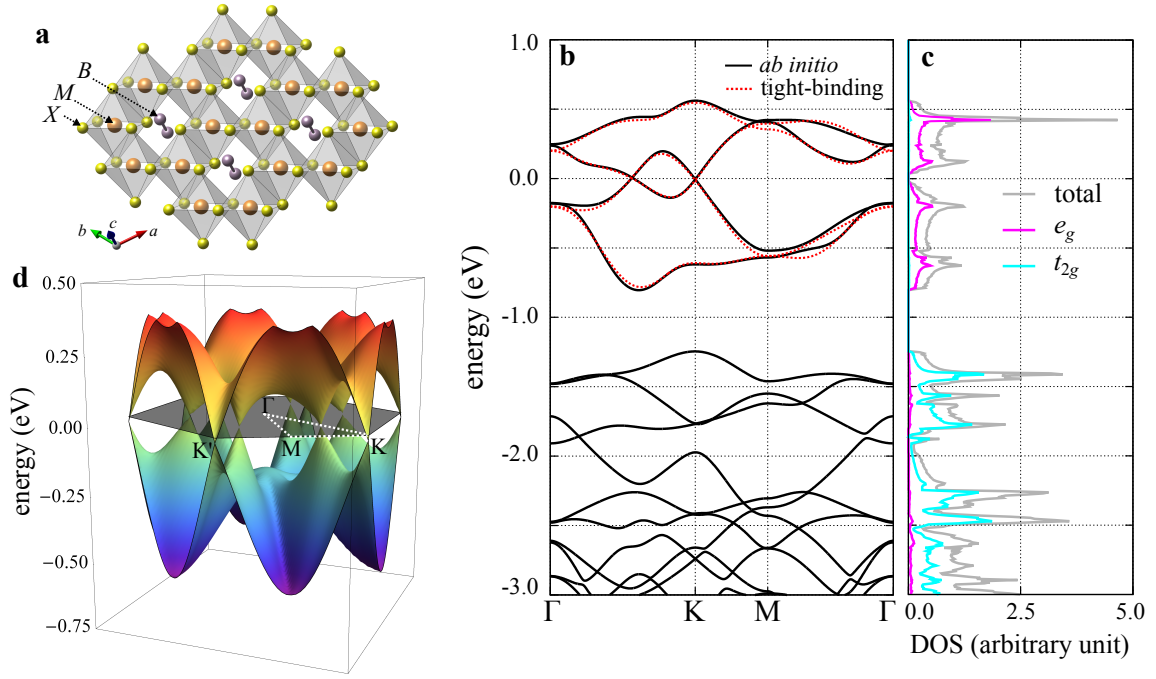


FIG. 1. **Lattice structure and electronic band structure of a monolayer TMT.** **a:** Schematic picture of a honeycomb-monolayer TMT, whose chemical formula is given as MBX_3 . The orange, purple, and yellow spheres denote the transition metals M , B , and chalcogens X , respectively. The gray octahedra indicate the edge-sharing MX_6 . M forms a honeycomb network. **b:** Electronic band structure of a monolayer PdPS_3 in the paramagnetic state without the SOC. The Fermi level is set to zero. The black solid lines represent the band dispersions obtained by *ab initio* calculations, while the red dotted ones are those by the tight-binding model for the e_g bands with the overlap integrals between MLWFs up to 5th neighbouring Pd cations (see Table I). **c:** Total density of states (DOS) and projected DOS for the Pd d orbitals. **d:** 3D plot of the two bands near the Fermi level. The multiple Dirac nodes are formed at the K and K' points and around the midpoints in the Γ -K lines in the 1st Brillouin zone indicated by the gray hexagon.

via the ligand p orbitals. Table I shows the overlap integrals between the two types of MLWFs for the Pd-Pd bonds up to 5th neighbours (see Fig. 2c). We confirm that the tight-binding analysis by using these overlap integrals well reproduce the *ab initio* band structure (see Fig. 1b). Interestingly, the most dominant overlap is not for nearest neighbours but the 3rd neighbours. This can be understood from almost forbidden d - p - d indirect hoppings between nearest neighbours (Fig. 2d) and substantial d - p - p - d indirect processes for the 3rd neighbours (Fig. 2e)[8].

(m, n)	R_1	R_2	R_3	R_4	R_5
$(3z^2 - r^2, 3z^2 - r^2)$	-87	-9	-38	4	-12
$(3z^2 - r^2, x^2 - y^2)$	0	22	0	-8	0
$(x^2 - y^2, 3z^2 - r^2)$	0	18	0	-8	0
$(x^2 - y^2, x^2 - y^2)$	-70	14	304	7	30

TABLE I. Overlap integrals between MLWFs, $\langle m, 0 | H | n, \mathbf{r} \rangle$, where H is the Hamiltonian of the system and $|m, \mathbf{r}\rangle$ is the d_m -like MLWF at site \mathbf{r} ($m = 3z^2 - r^2$ or $x^2 - y^2$). We take $\mathbf{r} = \mathbf{R}_i$ ($i = 1, 2, 3, 4$, or 5) illustrated in Fig. 2. The unit of overlap integrals is in meV.

The dominant 3rd neighbour overlaps explain the origin of the multiple Dirac cones. As well-known in graphene, the nearest neighbour overlaps produce the Dirac cones at the

zone corners, the K and K' points. This is also the case for the e_g electron systems[24]. On the other hand, the 3rd neighbour overlaps bring about Dirac cones at the additional six points inside the 1st Brillouin zone: the network of the 3rd neighbour bonds forms honeycomb superstructures with the lattice spacing twice longer than the original honeycomb network, as exemplified in Fig. 2c, which leads to new Dirac cones around the midpoints of the Γ -K lines (zone corners in the folded Brillouin zone). Thus, in our TMTs, the hidden honeycomb superstructures stemming from the orbital and geometric nature result in the multiple Dirac nodes.

Next, we discuss the effect of SOC. Although the orbital moment is quenched in the e_g manifold in an ideal octahedral crystal field, the SOC modifies the e_g electronic states through t_{2g} - e_g mixing in the presence of a distortion of MX_6 octahedra[24]. Indeed, we find that the Dirac nodes are gapped out by including the relativistic effect in the *ab initio* calculations, as shown in Fig. 3a. In this monolayer system, the dominant distortion is a trigonal one, which leads to an effective SOC proportional to $\tilde{\lambda} = \Delta_{\text{tri}}\lambda^2/\Delta^2$, where λ is the bare SOC constant for the d -electron manifold, and Δ and Δ_{tri} are the crystalline electric field splittings from the octahedral ligands and the trigonal distortion, respectively (see Supplementary information). Indeed, we confirm that the tight-binding analysis including the effective SOC well explains the band

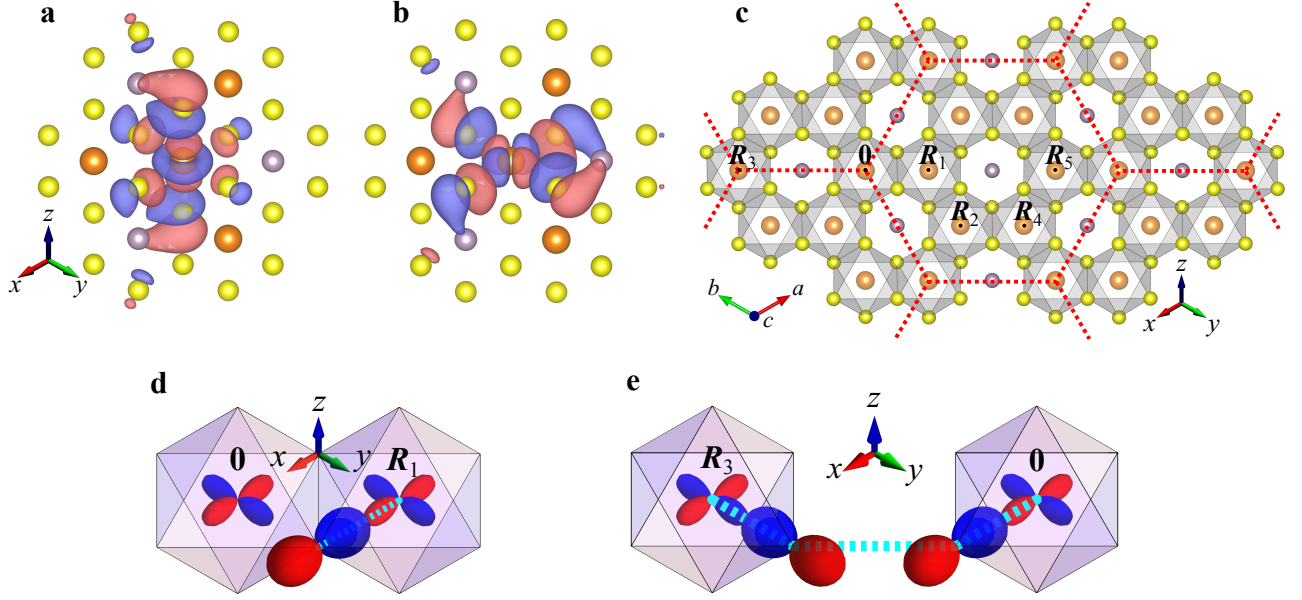


FIG. 2. e_g orbitals and their overlaps. **a** and **b**: Contour-surface plot of MLWFs, which are obtained from two initial states, $d_{3z^2-r^2}$ and $d_{x^2-y^2}$ orbitals, respectively. The red (blue) surfaces indicate the positive (negative) isosurface at +0.03 (-0.03). Both wave functions are not localized around the Pd site but fairly extended to neighbouring S sites. **c**: Atomic positions used in the calculation of overlap integrals summarized in Table I. R_i represents the i th neighbour site to the 0 site. The red dotted lines indicate a honeycomb superstructure composed of the 3rd neighbour bonds. **d** and **e**: Schematic pictures of 1st and 3rd neighbour hopping processes via the ligand p orbitals.

structure with the gapped Dirac nodes, as shown in Fig. 3a (see Method for details).

The result indicates that the Dirac gaps can be controlled through the crystalline symmetry. Here, we demonstrate it by tensile strain, which has been commonly used for two-dimensional vdW materials[25, 26]. Figure 3b shows the change in the Dirac gaps obtained by *ab initio* calculations while changing the in-plane lattice constant with fixed fractional coordinates of atoms. In the optimal structure (zero expansive ratio), the octahedra are slightly elongated in the out-of-plane direction. While the system is expanded in the in-plane directions, the Dirac gaps decrease and become minimal around 8-9% expansive ratio, where the trigonal distortion almost vanishes. Interestingly, the valley structures of the two massive Dirac cones are shifted individually by the tensile strain, as shown in Fig. 3c. These results indicate the flexible tunability of the massive Dirac cones.

Although the magnetism was studied for monolayer TMTs by *ab initio* calculations[8, 9], the previous works focused on the 3d compounds in which the SOC is irrelevant. We here investigate the synergetic effect of electron correlations and the SOC, both of which can be relevant in 4d and 5d compounds. We focus on two commensurate fillings, half filling (two e_g electrons per M) and 3/4 filling (three e_g electrons per M); the former corresponds to the situation discussed above, while the latter a chemical substitution of M by, e.g., Ag or Cd.

Figure 4a,b show the ground-state phase diagrams and the magnetic moments, obtained for the multi-orbital Hamil-

tonian constructed from the MLWF analysis by the mean-field approximation (see Method for details). At half filling (Fig. 4a), while increasing the electron correlations, the system exhibits a continuous phase transition from the paramagnetic Dirac semimetal to a Néel-type antiferromagnetic insulator (AFMI) with in-plane magnetic moments. Indeed, the *ab initio* calculations with allowing magnetic solutions predict that the lowest-energy state changes from the paramagnetic Dirac semimetal to AFMI while changing from weakly correlated $M = \text{Pt}$ to strongly correlated $M = \text{Ni}$; the $M = \text{Pd}$ case is close to the boarder (see Supplementary information). On the other hand, at 3/4 filling, the system shows a discontinuous phase transition from the paramagnetic metal to a ferromagnetic (FM) metal, and to a FM insulator with out-of-plane magnetic moments.

We find that the FM states at 3/4 filling acquires nontrivial topological nature. Figure 4c shows the band structure at $U = 1.5$ eV. The bands are split by the exchange field into the up-spin (red) and down-spin (blue) ones (see Supplementary information), and the lower six are occupied at 3/4 filling. Computing the Chern number for each band (see Method and Fig. 4c) and summing them for the occupied bands, we find that the FM insulator is a topologically-nontrivial ferromagnet with rather high Chern number $C = 4$. Figure 4d displays the wave-number dependence of the Berry curvature of the highest-occupied band with $C = 6$. The Berry curvatures shows spikes at the K and K' points and around the mid-points of the Γ -K lines. These anomalous contributions can

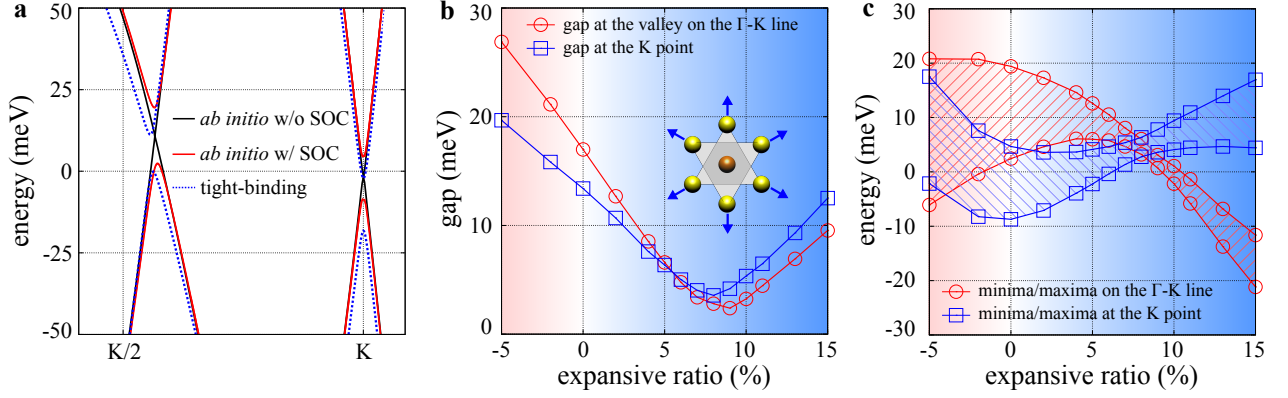


FIG. 3. **Effects of the SOC and tensile strain.** **a:** Enlarged figure of the electronic band structure of PdPS₃ near the Fermi level along the Γ -K line. The black (red) solid lines represent the band dispersions obtained by *ab initio* calculations neglecting (including) the SOC. The blue dotted ones are the dispersions for the tight-binding model with the overlap integrals of MLWFs up to 5th neighbouring Pd cations including the effective SOC with $\tilde{\lambda} = 15$ meV. **b:** The amplitudes of the Dirac gaps as functions of the expansive ratio of the in-plane lattice constant. Schematic image of tensile expansion is shown in the inset. **c:** The tensile-strain dependence of the two valley structures.

be traced back to the Dirac cones in the original semimetallic state. Thus, our results suggest that the multiple-Dirac semimetal can be turned into an unconventional topological ferromagnet with high Chern number by electron correlations and carrier doping.

We have theoretically uncovered two potential electronic properties of TMTs with *4d* and *5d* transition metals in the monolayer form. One is the highly-tunable multiple Dirac cones. This will bring about new transport phenomena, such as the unconventional Hall responses and the multiple valley operations. The other is the topological ferromagnetism with high Chern number driven by electron correlations and chemical doping. This will provide new candidates for quantized anomalous Hall insulators, whose multiple chiral edge modes might be used for a thin-film transmitter with high efficiency. We believe that the two features will stimulate further material exploration in *4d* and *5d* TMTs for delivering missing pieces in material science of atomically-thin films and the heterostructures.

Methods.

***ab initio* calculations.** For the electronic structure calculations, we used OpenMX code[27], which is based on a linear combination of pseudoatomic orbital formalism. We adopted the Perdew-Burke-Ernzerhof generalized gradient approximation (GGA) functional in density functional theory[28] and a $30 \times 30 \times 1$ k -point mesh for the calculations of the self-consistent electron density and the structure relaxation. We inserted vacuum space greater than 10 Å between monolayers. In the calculations without the SOC, we adopted the crystalline data in the bulk samples[17] as the initial condition and fully relaxed the primitive vectors and atomic positions in the unit cell with the convergence criterion 0.01 eV/Å about the interatomic forces. To discuss the SOC effect, we adopted a fully relativistic j -dependent pseudopotential and used the crystal structures obtained in the calculations without the SOC. The MLWFs[22, 23] were calculated via a code

implemented in OpenMX.

Multi-orbital Hubbard Hamiltonian and mean-field approximation. We studied the electron correlation effect for the multi-orbital tight-binding Hamiltonian constructed from the MLWF analysis, by adding the onsite Coulomb interactions and the effective SOC with $\tilde{\lambda} = 15$ meV (see Fig. 3a and Supplementary information). The Coulomb interaction is given by

$$H_{\text{int}} = \frac{1}{2} \sum_{mm'n'} U_{mm'n'} \sum_i \sum_{\sigma\sigma'} c_{im\sigma}^\dagger c_{in\sigma'}^\dagger c_{in'\sigma'} c_{im'\sigma}, \quad (1)$$

where $c_{im\sigma}^\dagger$ ($c_{im\sigma}$) is the creation (annihilation) operator of an electron for the i th site, orbital $m = d_{3z^2-r^2}$ or $d_{x^2-y^2}$, and spin $\sigma = \uparrow$ or \downarrow . Assuming the rotational symmetry of the Coulomb interaction, we set $U_{mmmm} = U$, $U_{mmnn} = U - 2J$, and $U_{nnmm} = U_{mmnn} = J$ ($m \neq n$), where U is the intraorbital Coulomb interaction and J is the Hund's coupling, respectively; we take $J/U = 0.2$ in the present calculations.

In the mean-field calculations, we adopted the standard Hartree-Fock approximation to decouple the onsite interaction terms. We took into account charge, spin, and orbital orders with the ordering vector $\mathbf{Q} = (0, 0)$ or (π, π) on the honeycomb lattice. We approximated the integration in the 1st Brillouin zone by the summation over 128×128 k points and determine the mean fields consistently within a precision of less than 10^{-6} .

Chern number and Berry curvature. We calculated the Berry curvature B_{nk} and the Chern number C_n for a n th band of the mean-field solution by using the standard Kubo formula given as[29]

$$B_{nk} = \sum_{m \neq n} \frac{2\text{Im} \left[\langle nk | \frac{\partial H_{\text{MF}}}{\partial k_x} | mk \rangle \langle mk | \frac{\partial H_{\text{MF}}}{\partial k_y} | nk \rangle \right]}{(E_{nk} - E_{mk})^2}, \quad (2)$$

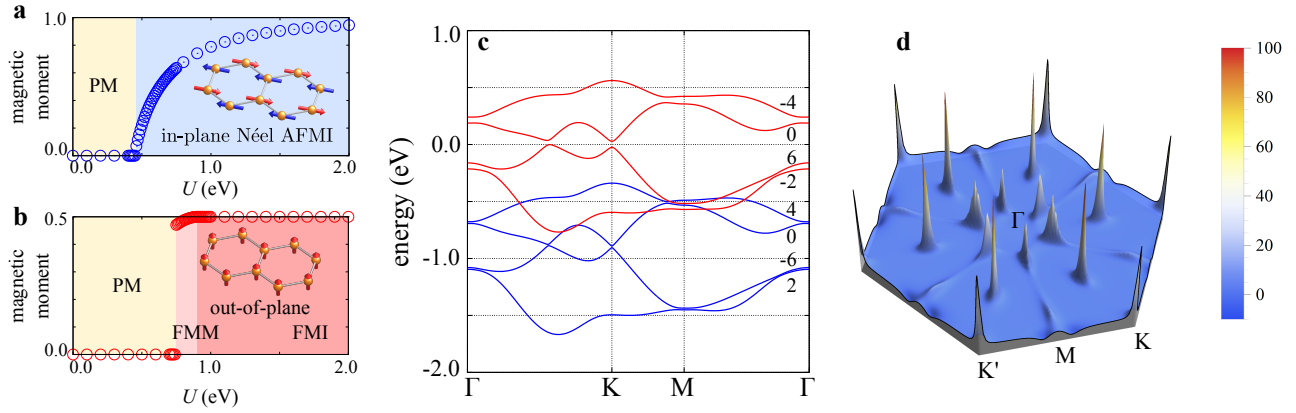


FIG. 4. **Magnetism induced by electron correlations.** **a** and **b**: Ground-state phase diagrams of the multi-orbital Hubbard model obtained by the mean-field approximation at half filling and 3/4 filling, respectively. PM, AFMI, FMM, and FMI represent the paramagnetic metal, antiferromagnetic insulator, ferromagnetic metal, and ferromagnetic insulator, respectively. The magnitude of magnetic moments is plotted in each magnetic phase. **c**: Electronic band structure for the FMI at $U = 1.5$ eV. The red and blue lines represent the up and down-spin bands, respectively, and the number on each band indicates the Chern number C . **d**: Wave-number dependence of the Berry curvature of the highest-occupied band with $C = 6$ in the 1st Brillouin zone.

$$C_n = \frac{2\pi}{\Omega} \sum_{\mathbf{k}} B_{n\mathbf{k}}, \quad (3)$$

where H_{MF} is the mean-field Hamiltonian, $E_{n\mathbf{k}}$ and $|n\mathbf{k}\rangle$ are the eigenvalue and eigenvector of the n th band with the wave vector \mathbf{k} in the mean-field solution, respectively, and Ω is the system volume. We note that as the mean-field Hamiltonian in the ferromagnetic state commutes with the spin operator, $B_{n\mathbf{k}}$ and C_n for each spin sector can be computed even in the presence of crossing between different spin bands (see Supplementary information).

Acknowledgements Y.S. is supported by the Japan Society for the Promotion of Science through the Program for Leading Graduate Schools (MERIT). The crystal structures and ML-WFs are visualized by using VESTA 3[30].

-
- [1] Novoselov, K. S., Geim, A. K., Morozov, S. V., Jiang, D., Katsnelson, M. I., Grigorieva, I. V., Dubonos, S. V. & Firsov, A. A. Two-dimensional gas of massless Dirac fermions in graphene. *Nature* **438**, 197-200 (2005).
 - [2] Castro Neto, A. H., Guinea, F., Peres, N. M. R., Novoselov, K. S. & Geim, A. K. The electronic properties of graphene. *Rev. Mod. Phys.* **81**, 109 (2009).
 - [3] Splendiani, A., Sun, L., Zhang, Y., Li, T., Kim, J., Chim, C.-Y., Galli, G. & Wang, F. Emerging Photoluminescence in Monolayer MoS_2 . *Nano Lett.* **10**, 1271 (2010).
 - [4] Wang, Q. H., Kalantar-Zadeh, K., Kis, A., Coleman, J. N. & Strano, M. S. Electronics and optoelectronics of two-dimensional transition metal dichalcogenides. *Nature Nanotech.* **7**, 699-712 (2012).
 - [5] Xu, X., Yao, W., Xiao, D. & Heinz, T. F. Spin and pseudospins in layered transition metal dichalcogenides. *Nature Phys.* **10**, 343-350 (2014).
 - [6] Geim, A. K. & Grigorieva, I. V. Van der Waals heterostructures. *Nature* **499**, 419-425 (2013).
 - [7] Novoselov, K. S., Mishchenko, A., Carvalho, A. & Castro Neto, A. H. 2D materials and van der Waals heterostructures. *Science* **353**, aac9439 (2016).
 - [8] Sivadas, N., Daniels, M. W., Swendsen, R. H., Okamoto, S. & Xiao, D. Magnetic ground state of semiconducting transition-metal trichalcogenide monolayers. *Phys. Rev. B* **91**, 235425 (2015).
 - [9] Chittari, B. L., Park, Y., Lee, D., Han, M., MacDonald, A. H., Hwang, E. & Jung, J. Electronic and magnetic properties of single-layer MPX_3 metal phosphorous trichalcogenides. *Phys. Rev. B* **94**, 184428 (2016).
 - [10] Du, K.-z., Wang, X.-z., Liu, Y., Hu, P., Utama, M. I. B., Gan, C. K. Xiong, Q. & Kloc, C. Weak Van der Waals Stacking, Wide-Range Band Gap, and Raman Study on Ultrathin Layers of Metal Phosphorus Trichalcogenides. *ACS Nano* **10**, 1738 (2016).
 - [11] Lin, M.-W., Zhuang, H. L., Yan, J., Ward, T. Z., Puzos, A. A., Rouleau, C. M., Gai, Z., Liang, L., Meunier, V., Sumpster, B. G., Ganesh, P., Kent, P. R. C., Geoghegan, D. B., Mandrus, D. G. & Xiao, K. Ultrathin nanosheets of CrSiTe_3 : a semiconducting two-dimensional ferromagnetic material. *J. Mater. Chem. C* **4**, 315 (2016).
 - [12] Kuo, C.-T. Neumann, M., Balamurugan, K., Park, H. J., Kang, S., Shiu, H. W., Kang, J. H., Hong, B. H., Han, M., Noh, T. W. & Park, J.-G. Exfoliation and raman spectroscopic fingerprint of few-layer NiPS_3 Van der Waals crystals. *Sci. Rep.* **6**, 20904 (2016).
 - [13] Lee, J.-U., Lee, S., Ryoo, J. H., Kang, S., Kim, T. Y., Kim, P., Park, C.-H., Park, J.-G. & Cheong, H. Ising-Type Magnetic Ordering in Atomically Thin FePS_3 . *Nano Lett.* **16**, 7433 (2016).
 - [14] Li, X., Cao, T., Niu, Q., Shi, J. & Feng, J. Coupling the valley degree of freedom to antiferromagnetic order. *Proc. Natl. Acad. Sci. U.S.A.* **110**, 3738 (2013).
 - [15] Cheng, R., Okamoto, S. & Xiao, D. Spin Nernst Effect of Magnons in Collinear Antiferromagnets. *Phys. Rev. Lett.* **117**, 217202 (2016).
 - [16] Sivadas, N., Okamoto, S. & Xiao, D. Gate-Controllable Magneto-optic Kerr Effect in Layered Collinear Antiferromagnets. *Phys. Rev. Lett.* **117**, 267203 (2016).

- [17] Klingen, W., Ott, R. & Hahn, H. Über die Darstellung und Eigenschaften von Hexathio- und Hexaselenohypodiphosphaten. *Z. Anorg. Allg. Chem.* **396**, 271 (1973).
- [18] Brec, R. Review on structural and chemical properties of transition metal phosphorous trisulfides MPS_3 . *Solid State Ionics* **22**, 3 (1986).
- [19] Ouvrard, G., Sandre, E. & Brec, R. Synthesis and crystal structure of a new layered phase: The chromium hexatellurosilicate $\text{Cr}_2\text{Si}_2\text{Te}_6$. *J. Solid State Chem.* **73**, 27 (1988).
- [20] Carteaux, V., Brunet, D., Ouvrard, G. & Andre, G. Crystallographic, magnetic and electronic structures of a new layered ferromagnetic compound $\text{Cr}_2\text{Ge}_2\text{Te}_6$. *J. Phys.: Cond. Matter* **7**, 69 (1995).
- [21] Greenwood, N. N. & Earnshaw, A. *Chemistry of the Elements*, Second Edition (Butterworth-Heinemann, 1997).
- [22] Marzari, N. & Vanderbilt, D. Maximally localized generalized Wannier functions for composite energy bands. *Phys. Rev. B* **56**, 12847 (1997).
- [23] Souza, I., Marzari, N. & Vanderbilt, D. Maximally localized Wannier functions for entangled energy bands. *Phys. Rev. B* **65**, 035109 (2001).
- [24] Xiao, D., Zhu, W., Ran, Y., Nagaosa, N. & Okamoto, S. Interface engineering of quantum Hall effects in digital transition metal oxide heterostructures. *Nature Commun.* **2**, 596 (2011).
- [25] Lee, C., Wei, X., Kysar, J. W. & Hone, J. Measurement of the Elastic Properties and Intrinsic Strength of Monolayer Graphene. *Science* **321**, 385-388 (2008).
- [26] Guinea, F., Katsnelson, M. I. & Geim, A. K. Energy gaps and a zero-field quantum Hall effect in graphene by strain engineering. *Nature Phys.* **6**, 30-33 (2010).
- [27] See <http://www.openmx-square.org/>.
- [28] Perdew, J. P., Burke, K. & Ernzerhof, M. Generalized Gradient Approximation Made Simple. *Phys. Rev. Lett.* **77**, 3865 (1996).
- [29] Thouless, D. J., Kohmoto, M., Nightingale, M. P. & den Nijs, M. Quantized Hall Conductance in a Two-Dimensional Periodic Potential. *Phys. Rev. Lett.* **49**, 405 (1982).
- [30] Momma, K. & Izumi, F. VESTA3 for three-dimensional visualization of crystal, volumetric and morphology data. *J. Appl. Cryst.* **44**, 1272 (2011).